Geoscience Frontiers 11 (2020) 855–870

HOSTED BY

Contents lists available at ScienceDirect

Geoscience Frontiers

journal homepage: www.elsevier.com/locate/gsf

Research Paper

Dating long thrust systems on Mercury: New clues on the thermal evolution of the planet

L. Giacomini [a,*], M. Massironi [b], V. Galluzzi [a], S. Ferrari [c], P. Palumbo [d]

[a] INAF-IAPS, Istituto di Astrofisica e Planetologia Spaziali, Via Fosso Del Cavaliere 100, Rome, 00133, Italy
[b] Dipartimento di Geoscienze, University of Padova, Via G. Gradenigo 6, Padova, 35131, Italy
[c] Center of Studies and Activities for Space (CISAS) "G. Colombo", University of Padova, Via Venezia 15, Padova, 35131, Italy
[d] Dipartimento di Scienze e Tecnologie, University of Naples "Parthenope", Centro Direzionale, Isola C4, Napoli, 80143, Italy

ARTICLE INFO

Handling Editor: Richard M Palin

Keywords:
Mercury
Thrust systems
Crater counting
Thermal evolution
Planetary geology
Structural geology

ABSTRACT

The global tectonics of Mercury is dominated by contractional features mainly represented by lobate scarps, high relief ridges, and wrinkle ridges. These structures are the expression of thrust faults and are linear or arcuate features widely distributed on Mercury. Locally, these structures are arranged in long systems characterized by a preferential orientation and non-random spatial distribution. In this work we identified five thrust systems, generally longer than 1000 km. They were named after the main structure or crater encompassed by the system as: Thakur, Victoria, Villa Lobos, Al-Hamadhani, and Enterprise. In order to gain clues about their formation, we dated them using the buffered crater counting technique, which can be applied to derive the ages of linear landforms such as faults, ridges and channels. To estimate the absolute age for the end of the thrust system's activity, we applied both Le Feuvre and Wieczorek Production Function and Neukum Production Functions. Moreover, to further confirm the results obtained with the buffered crater counting method, the classic stratigraphic approach has been adopted, in which a faulted and an unfaulted craters were dated for each system. The results gave consistent ages and suggested that the most movements along major structures all over Mercury most likely ended at about 3.6–3.8 Ga. This gives new clues to better understand the tectonics of the planet and, therefore, its thermal evolution. Indeed, the early occurrence of tectonic activity in the planet's history, well before than predicted by the thermophysical models, coupled with the orientation and spatial distribution of the thrust systems, suggests that other processes beside global contraction, like mantle downwelling or tidal despinning, could have contributed to the first stage of the planet's history.

1. Introduction

When the NASA Mariner 10 spacecraft approached Mercury in 1974, it revealed a planet with widespread tectonic landforms on its surface. About forty years later, this was further confirmed by the NASA MESSENGER (MErcury Surface, Space ENvironment, GEochemistry and Ranging) mission that performed global mapping of the planet, revealing that Mercury's tectonic fabric is widely distributed on the entire surface.

The observed tectonic features are mainly represented by structures named lobate scarps, high relief ridges, and wrinkle ridges, which are different expressions of compressive stress acting on the surface (Strom et al., 1975).

In particular, lobate scarps are surface expression of thrust faults, linear or arcuate in plan view. They are generally asymmetric in cross section with a steeply sloping scarp face and a gently sloping back limb (e.g. Watters et al., 2015), probably representing a monocline or asymmetric hanging-wall anticline atop a blind or surface-breaking thrust fault (Byrne et al., 2014; Massironi et al., 2015). High relief ridges are less common than lobate scarps and more symmetric in cross section (e.g. Dzurisin, 1978). These features exhibit both horizontal shortening and vertical offset of the wall. Finally, wrinkle ridges are broad, low-relief arches with a narrow superposed ridge. They are interpreted to be the result of a combination of folding and faulting, i.e. an anticlinal fold above a blind thrust fault (Byrne et al., 2014; Watters et al., 2015 and references therein).

The global distribution of these contractional features led several

* Corresponding author.
E-mail address: lorenza.giacomini@inaf.it (L. Giacomini).
Peer-review under responsibility of China University of Geosciences (Beijing).

https://doi.org/10.1016/j.gsf.2019.09.005
Received 28 February 2019; Received in revised form 16 July 2019; Accepted 25 September 2019
Available online 10 October 2019

authors to hypothesize that they could be the expression of two major processes: global contraction (Watters et al., 1998, 2009a; Watters and Nimmo, 2010), tidal despinning (Burns, 1976; Melosh, 1977; Melosh and Dzurisin, 1978; Melosh and McKinnon, 1988), or a combination of the two (Pechmann and Melosh, 1979; Dombard and Hauck, 2008; Matsuyama and Nimmo, 2009; Beuthe, 2010; Klimczak et al., 2015). More recently, mantle convection has also been invoked as a possible mechanism (King, 2008; Marchi et al., 2009; Massironi et al., 2015).

Global contraction results from the progressive cooling of planet's interior. The decrease of the internal temperature causes phase changes such as those associated with the solidification of the inner core (e.g. Solomon, 1976, 1977; Schubert et al., 1988; Hauck et al., 2004; Grott et al., 2011). If global contraction acted alone, it should have caused global, horizontally isotropic compressional stresses and a uniformly distributed population of randomly oriented lobate scarps (Klimczak et al., 2015; Watters et al., 2015).

Tidal despinning, instead, is the slowing of an initially rapid rotation accompanied by a relaxation of the equatorial tidal bulge. Initially, this process was thought to cause a distinctive latitude–dependent pattern with an equatorial zone of N–S oriented thrust faults, a middle-latitude zone characterized by strike-slip faults with a NE–SW and NW–SE orientations, and, finally, polar regions with E–W oriented normal faults (Melosh and Dzurisin, 1978). Recently, however, Klimczak et al. (2015) took into account the elastic proprieties of lithosphere and concluded that tidal despinning alone would only produce a global set of opening-mode fractures with no preferred orientation at the poles, with progressively preferred E–W orientation towards the equator.

Neither global contraction nor tidal despinning, however, fits with the observed global pattern of Mercury, which shows a prevalent N–S orientated thrust faults on the equatorial areas and a slight E–W orientated thrust faults at the higher latitudes (Watters et al., 2015). If global contraction and tidal despinning operated simultaneously for a certain time span, the resulting fabric would include N–S oriented thrusts at the equator and middle latitude and randomly oriented thrusts at the poles (Klimczak et al., 2015).

Alternatively, mantle convection suggests that compressional stresses along zones of mantle downwelling would enhance the localization of N–S oriented faults at lower latitude and E–W faults at higher latitude (King, 2008; Marchi et al., 2009).

Improved knowledge of the duration and timing of these processes could help to understand which mechanism – or combination of mechanism – is responsible for the formation of the observed pattern of tectonic structures on Mercury. To this end, we identified several long thrust systems, distributed over the planet's surface (Fig. 1), and we determined their ages, not only through stratigraphic relationships, but also with the absolute model age assessments through crater size-frequency distribution (CSFD) measurements and using the Buffered Crater Counting (BCC) technique.

2. Data and methods

The first phase of this work was to identify the thrust systems, searching for a series of clustered thrust segments, linked together at the surface and characterized by a consistent trend and vergence. Based on this, we can state that these thrusts formed in response to the same forces. Since our aim is to study the stress regime acting on the planet surface at a regional scale, we considered systems with a considerable length, generally exceeding 1000 km. In addition, this allows collecting a significant number of craters, obtaining a good statistic from the crater counting.

A change of vergence with respect to the main structures can be locally observed in correspondence of craters. This can be due to pre-existing anisotropies potentially related to the craters themselves, causing the formation of faults with an opposite vergence. Thrusts showing coherent orientation but an opposite vergence with respect to the primary faults, and that do not represent back-thrusts of the main structures or are not related to preexisting craters, were not included in the systems. Moreover, we did not take into account wrinkle ridges located in the widespread smooth plains of the northern latitudes and Caloris basin surroundings (Denevi et al., 2013), since they could have been developed in response also of loading-induced stresses, which depend by the thickness and distribution of smooth plain material (Watters et al., 2009b).

To identify these systems we used the MESSENGER MDIS (Mercury Dual Imaging System) monochrome global mosaic with a spatial resolution of 250 *m*/pixel compiled using NAC (Narrow Angle Camera) and WAC (Wide Angle Camera) images acquired in the filter centered at 750 nm (Fig. 1).

Once the systems were detected, we used the MDIS map projected basemap reduced data record (BDR) monochrome mosaics with a higher spatial resolution of 166 *m*/pixel as basemap to outline each specific thrust system. The BDR mosaic is made of NAC and WAC 750-nm images illuminated with a solar incidence angle around 74°. The basemap mosaics illuminated with high solar incidence angle both from east (HIE) and west (HIW) were also considered to better distinguish the structures. For each thrust system the mosaics were processed with USGS Integrated Software for Imagers and Spectrometers (ISIS) and reprojected with ArcGIS in order to center them at the latitude and longitude of the

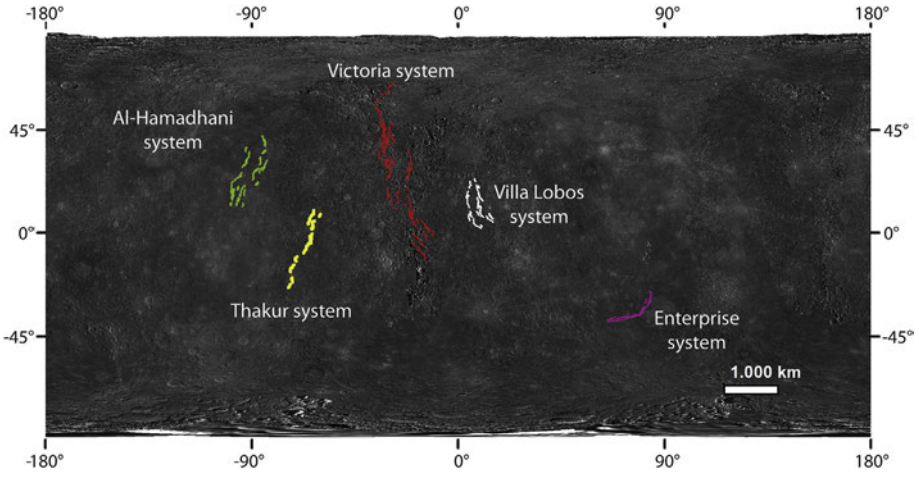

Fig. 1. Global view of the five thrust systems analyzed and dated in this work. The background is the MDIS global mosaic (spatial resolution 250 *m*/pixel) in equirectangular projection.

feature. This procedure was performed to avoid distortion and the consequent alteration of the final length of the fault systems. Finally, the tectonic structures were digitized as vector shapefiles.

2.1. The buffered crater counting technique (BCC) and the stratigraphic method

To date the thrust systems we used the BCC technique, a method developed by Tanaka (1982) to derive the age of linear features (such as faults and channels) and subsequently employed by Wichman and Schultz (1989) to study large-scale Martian extensional tectonics. More recently, this technique has been used by Fassett et al. (2008), Hoke and Hynek (2009), and Bouley et al. (2010) to determine the age of Martian valley networks, and by Kneissl et al. (2015) to date Martian graben systems. Giacomini et al. (2015) and Galluzzi et al. (2019) applied the method on Mercury to date the Blossom and Victoria thrust systems, respectively, whereas Fegan et al. (2017) dated some Hermean basin-edge lobate scarps. Finally, this technique has also been used on lunar wrinkle ridges (Clark et al., 2017; Yue et al., 2017), and lobate scarps (Senthil Kumar et al., 2016; van der Bogert et al., 2018).

The BCC method assumes that it is possible to determine a stratigraphic relationship between lineaments and craters. Indeed, only craters formed after the lineaments can be considered in the count to date the end of thrust systems' activity. To estimate such a stratigraphic relationship, two different approaches can be followed. The broadest one considers all the craters superposed on the structures as well as those whose ejecta lay over the lineaments. In this latter case, craters located at a certain distance from the lineaments are also considered in the count. This allows more craters to be considered. However, quite often it is not easy to discern whether the crater ejecta superimpose a lineament or not, with a consequent greater uncertainty in the age estimation. The second approach is more stringent and considers only those craters whose rim intersects the lineaments.

In this work, we adopted the latter approach in order to be more confident that the counted craters are formed after the structures.

To perform the BCC, the "CraterTool" software developed by Kneissl et al. (2011) was employed. This application automatically calculates the required buffer width for each crater and creates buffer polygons around the linear features, merging the overlapping areas.

With the CraterTool software the width of the buffer can be chosen from 1R to 3R (R = radius of crater), depending on which approach has been adopted. In the case of 1R, no crater ejecta are taken into account. On the contrary, in the case of 2R and 3R, the extensions of crater's ejecta of two or three radii (from the center of the crater) are considered, respectively.

In this work, although during the selection of craters we adopted the more stringent method (i.e. only craters whose rim overlays the structures), we considered also the ejecta of the craters to estimate the buffer areas. Indeed, we assumed that every crater formed its ejecta during the impact; therefore we held that they should be included in the estimate of the buffered areas. Hence, we chose a buffer width equal to 2R. Actually, Melosh (1989) states that crater ejecta can extend up to one diameter from the crater rim (i.e. 3R from the crater center) but, according to Gault et al. (1975), the ejecta on Mercury extent up to 2R from the center of the crater.

Therefore, the buffered area (A) can be expressed as:

$$A = 2(\mathrm{Sbuffer}) \times L$$

Where L is the length of the structure and Sbuffer is:

$$\mathrm{Sbuffer} = 2R + 0.5W$$

W being the width of the linear feature that is mapped as an elongated polygon. Such polygon needs to include surfaces formed during the same event. Therefore, to draw it, we considered as thrust width just the thrust's scarp, where we are more confident that preexisting craters were erased. On the contrary, if we include in this polygon also thrust-related landforms (e.g. anticlinal folds associated with thrusts), we cannot assure that all of the craters located within these areas effectively postdate the thrust, since some preexisting craters could have persisted. Consequently, also some craters predating the structures could be counted, with the overestimation of the system's age.

In this work the width for all the structures was considered as 2 km, which is the minimum width that includes the thrust's scarps. We performed also some tests considering a width of 1 km and 4 km but no significant changes in the final results were obtained.

To be more conservative, we decided to consider also the case where no crater ejecta have been taken into account (Sbuffer = R+0.5W), in order to compare the results obtained considering the two different approaches on calculating the buffer areas.

Since the thrust systems under study are considerably long, geodesic buffers were applied in order to avoid projection distortions and consequent erroneous calculations of buffered areas. Indeed, the geodesic buffer takes into account the curvature of the planet's surface, giving more accurate buffer offsets and, therefore, more precise buffered areas, in particular for features that cover long distances in latitude.

As highlighted in previous works (Wichman and Schultz, 1989; Fassett et al., 2008; Bouley et al., 2010), one of the most important constraints of the BCC method is the limited number of crater statistics for small features. However, as all the considered systems are quite long (from 800 km to 3500 km), the counts involved a large area and the crater count-derived statistics can be considered robust. Recently, BCC technique was also applied on small scarps on the Moon (van der Bogert et al., 2018). Despite the modest lengths, BCC results show generally a good agreement with the traditional CSFD measurement (van der Bogert et al., 2018), suggesting that the technique is efficient on dating also small features, if a sufficient superposing craters are collected. This was allowed by the high resolution of the satellite images available for the lunar surface (e.g. up to 0.50 *m*/pixel for LROC images), which permitted to obtain, in most of the cases, a solid statistic.

After the buffer crater counts, the resulting crater size-frequency data were exported with the CraterTools software in a format compatible with the Craterstats analysis software (Michael and Neukum, 2010) used to determine absolute model ages for the thrust systems. Craterstats allows an estimation of the age by performing a best fit of the CSFD and then providing the absolute model age value with the relative errors (based on the statistics of Poisson cratering process related to the nonlinear chronology functions of the models; Michael and Neukum, 2010). The best fit was performed considering craters diameters larger than 2–3 km, and minimizing the relative errors. The smaller craters were avoided since a progressive fall-off is observed, which is likely due to the resolution limit of used images (Michael and Neukum, 2010). Moreover, considering small craters can lead to the inclusion of secondaries. The contribution of secondary craters within the smaller diameter ranges (<10 km on Mercury; e.g. Strom et al., 2018) is still a matter of debate. Indeed, for some authors secondary craters dominate the small crater population, whereas, according to other authors, secondaries are negligible or, at least, they are integrated in the crater chronology, so their contribution has already been included in the crater statistics (Xiao, 2018 and reference therein). In order to avoid as much as possible the influence of secondaries, we excluded from our counts all the craters that are arranged in clusters or chains and that show an irregular rim or shape, signs of low energy impacts, which are likely the results of secondary impacts (Melosh, 1989).

Finally, we also performed a more classic stratigraphic dating, in order to validate the results of the BCC method. For each system, one crater that has been cut by thrusts and one crater that superposes the thrusts were dated. This allows a maximum and a minimum age limit of the thrust activity to be obtained, respectively. To gain the narrowest time range for the thrust system activity, we should date the youngest among the faulted craters and the oldest among the unfalted craters. To reach this aim it is preferable to choose a faulted crater showing a less cratered floor (for the maximum limit) and an unfaulted crater showing a

more cratered floor (for the minimum limit). However, this is not always possible since we had to avoid craters affected by secondaries of subsequent craters that could invalidate the statistics. Consequently, often the time gap between the age obtained with the BCC method and maximum and minimum age limits is very wide. This implies that the chosen faulted craters can be formed considerably before the thrust occurrence and, on the contrary, that unfaulted craters could be emplaced well after the end of thrust system activity. Although maximum and minimum limits obtained with the stratigraphic method do not reflect the effective age of the systems' activity, they provide a time range that can be used to test the BCC technique, since the results of the two different approaches need to be concordant.

In several cases, the chosen craters have a limited area, thus, to date them we employed single MDIS images at higher resolution, which have been calibrated and georeferenced with ISIS software.

A limited area also implies that often the CSFD mainly includes small diameters, less than 10 km, implying that possible far field secondaries can contribute to the crater population. In order to minimize their contribution we consider, for the stratigraphic study, craters that are far from the largest basins, whose secondary craters could have affected the surrounding areas. Nevertheless, during the count, craters with irregular morphologies and/or arranged in chains and clusters have been excluded and areas occupied by them were clipped and removed from the counting area (Platz et al., 2013).

Regarding the minimum age limit, in some cases the considered craters are very young (i.e. the case of Thakur and Enterprise thrust system). Although the diameters considered in the count have diameters <1 km, we can be confident that the CSFDs are not affected by secondaries since the craters emplaced after the LHB, when the formation of large craters was rarer, and the contribution of far field secondary impact craters is less significant (Strom et al., 2018).

In fact, the CSFDs resulting from the counts do not show an evident steepening for small diameters, suggesting that the effects of secondaries are negligible.

2.2. Crater chronology models

To obtain an absolute model age of both the lineaments and the crater floors we used two different models: the model Production Function proposed by Le Feuvre and Wieczorek (hereafter called LWPF) (Le Feuvre and Wieczorek, 2011) and the Neukum Production Function (NPF) (Neukum et al., 2001a).

Neukum et al. (2001a) derived the Mercurian Production Function from the lunar Neukum Production Function (Neukum, 1983; Neukum and Ivanov, 1994; Neukum et al., 2001a, b), by applying a scaling law relative to the impactor flux and its velocity distribution, and by taking into account the differences in gravitational acceleration and target properties (Hartmann, 1977; Strom and Neukum, 1988; Neukum et al., 2001a, b). Since NPF was the most known and used chronological model in the past, we decided to use also this model to give a basis of comparison with the ages previously calculated for Mercurian features.

LWPF is a more recent model that takes into account the impactor flux that affected the planet surface as well as the different rheological proprieties of the surface itself.

It assumes that the impactor SFD is the same for all the planets and the impact probability is independent of the projectile size. To derive the CSFD from the impactor SFD, Le Feuvre and Wieczorek (2011) used the porous scaling law and the non-porous scaling law of Holsapple and Housen (2007), based on the target rheology. In the LWPF only the gravity regime is considered on the scaling law and therefore tensile strengths of rocks are negligible (this holds for crater larger than a few hundred meters in rocks and larger than a few meters in consolidated soil). The transition between porous and non-porous scaling law is considered linear (see Le Feuvre and Wieczorek, 2011). The choice between the two different scaling laws proposed by Holsapple and Housen (2007) has important implications on the resulting age. In fact, the same measured CSFD will give a substantially older age if fitted assuming a cohesive soil/porous material rather than a non-porous/hard rock target. This considerable age difference results from the fact that porous target dissipates the impactor energy more efficiently than does the non-porous one. Therefore, for given impactor masses and velocities, craters formed on porous material will be smaller than those formed on hard rock (Holsapple and Housen, 2007; van der Bogert et al., 2017 and reference therein).

In this work, we decided to consider the LWPF porous scaling law results, rather than the non-porous ones, for the reasons discussed below.

The thrust systems considered cross prevalently intercrater plains, densely cratered and then highly fractured. Moreover, the greater part of craters considered in the count has generally moderate dimensions, with diameters ranging between 1 km and 20 km. Such range of crater diameters is lower than that proposed by Le Feuvre and Wieczorek (2011) for non-porous regime (i.e. diameter >20 km). Indeed, according to Holsapple (1993), for complex craters, the relationship between the observed crater diameter (D) and the transient crater diameter (D_t) is:

$$\frac{D}{D_t} = 1.02\left(\frac{D}{D_*}\right)^{0.079}$$

where D_* is the transition diameter between simple and complex crater, that on Mercury corresponds to 10.3 km (Pike, 1978).

The ratio between the depth (H_t) and the diameter (D_t) of the transient crater is estimated to be between 1/3 and 1/4 (Melosh and Ivanov, 1999). Then, for craters with an observed diameter of 20 km, the maximum excavation depth, H_t, ranges between 6.2 km and 4.6 km.

Schultz (1993) estimated a thickness of 4.5 km for the upper fractured bedrock layer on Mercury, due to the cooling joints and fractures of basalts. However, it is likely that the subsequent impacts caused a

Table 1
Model ages and maximum and minimum age limits of the five thrust systems investigated in this work.

	LWPF (porous scaling law)	LWPF (non-porous scaling law)	NPF
Thakur system:	3.7 (+0.03/–0.06) Ga	990 (±300) Ma	3.6 (+0.04/–0.06) Ga
Maximum age limit (Thakur crater)	3.7 (+0.01/–0.02) Ga	150 (±10) Ma	3.8 (±0.02) Ga
Minimum age limit	84 (±20) Ma	2.6 (±0.5) Ma	260 (±60) Ma
Victoria system:	3.7 (±0.02) Ga	1.0 (±0.2) Ga	3.8 (±0.02) Ga
Maximum age limit (Donne crater)	3.8 (+0.01/–0.02) Ga	300 (±40) Ma	3.9 (±0.02) Ga
Minimum age limit	2.4 (±0.4) Ga	49 (±9) Ma	3.5 (+0.05/–0.08) Ga
Villa Lobos system:	3.6 (+0.09/–0.8) Ga	720 (±300) Ma	3.6 (+0.06/–0.01) Ga
Maximum age limit	3.7 (+0.02/–0.03) Ga	990 (±300) Ma	3.9 (+0.04/–0.05) Ga
Minimum age limit (Kyosai crater)	1.3 (±0.4) Ga	32 (±9) Ma	3.4 (+0.1/–0.5) Ga
Al Hamadhani system:	3.7 (+0.02/–0.03) Ga	970 (±200) Ma	3.8 (±0.03) Ga
Maximum age limit	3.8 (+0.01/–0.02) Ga	760 (±200) Ma	3.9 (+0.02/–0.03) Ga
Minimum age limit	100 (±40) Ma	2.1 (±0.7) Ma	300 (±100) Ma
Enterprise system:	3.7 (+0.03/–0.04) Ga	2.1 (±0.7) Ga	3.8 (+0.05/–0.08) Ga
Maximum age (Rembrandt basin)	3.8 (±0.007) Ga	3.1 (±0.3)Ga	3.85 (±0.1) Ga (from Ferrari et al., 2015)
Minimum age	950 (±200) Ma	27 (±7) Ma	2.0 (±0.4) Ga

Thrust systems and craters have been dated using both Le Feuvre and Wieczorek Production function (LWPF) and Neukum Production Function (NPF). For LWPF both porous and non-porous scaling law results have been reported, although just the formers have been considered in this work (see text for more details).

thickening of this fractured bedrock, especially in the old intercrater plains. Therefore, it is probable that all the counted craters involved only the upper heavily fractured surface of the planet.

This evidence led us to consider the porous scaling law as the most suitable for our age estimation.

This is further confirmed by a comparison between the LWPF best fits performed with porous and non-porous scaling law. Indeed, we observed that, for all the systems, the porous isochrons fit better with our CSFDs rather than the non-porous ones, giving smaller errors on the age estimation. Finally, if we consider the non-porous scaling law, for the Thakur and Victoria systems the relationship between thrust's age and maximum age limit would not be respected.

The porous material scaling law was employed also to date the crater floors, and smooth plains infilling the basin. Although in this latter case non-porous material seems to be the most appropriate scaling law to use, also in this case basalt materials are highly fractured at the surface due to pervasive jointing by cooling of the lavas (Schultz, 1993). Therefore, a cohesive soil/porous material scaling law is more representative of these types of terrain considering the small dimension of the counted craters (less than 10 km) (Giacomini et al., 2015).

3. Thrust systems description and their model age estimation

Based on the criteria described in Section 2, we detected five long thrust systems. We refer here to each of them by the name of a prominent feature encompassed by the system, such a rupes or large crater. The following names of the system are informal (i.e. not included in the USGS Gazetteer of Planetary Nomenclature).

The ages obtained for each thrust system, considering the Sbuffer = 2R + 0.5W and the LWPF and NPF age models, are listed in Table 1. For LWPF, both the porous material and the non-porous material scaling law are reported in that table. However, in the following sections only porous scaling law results are considered and discussed. The best fits of CSFDs with LWPF non-porous scaling law are included in the supplementary material.

The ages obtained considering the Sbuffer = R+0.5W did not show significant difference with respect to the first approach and they are reported in the supplementary material as well.

Since only the undeformed craters that overlap the thrust were counted, by applying the BCC technique we estimated the age of the final stage of thrust activity. In addition to the BCC results, also the maximum and minimum age limit, obtained by dating a faulted and an unfaulted crater respectively, are reported. To gain maximum and minimum ages a traditional CSFD measurement was used.

3.1. Thakur system

This system, located between 9.93°N and 23.78°S, 74.13°W and 60.10°W, is constituted by eighteen structures for a total length of 1600 km. It cuts a crater of 104 km of diameter, called Thakur. Hence, we refer here to this system as "Thakur thrust system" (Fig. 2).

The structures cut different terrains, from intercrater plains to smooth plains, these latter with modest extension and emplaced within largest craters.

The tectonic structures are uniformly NNE–SSW oriented and their slope asymmetry suggests a NW vergence. Locally, in particular in

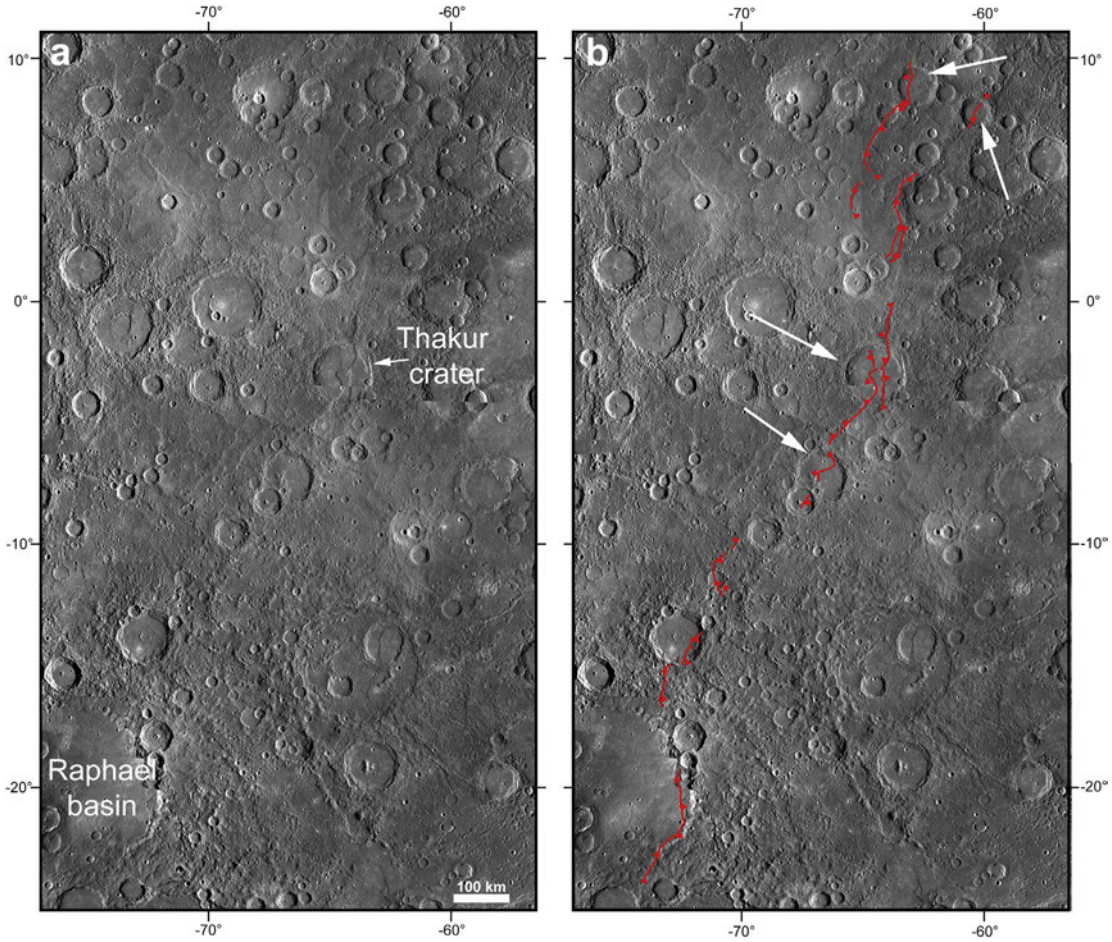

Fig. 2. Thakur thrust system, named after the Thakur crater, which is cut by one of the structures included in the system (a). (b) Thakur system's structures (in red; triangles indicate the dip direction of the thrust), show a NW vergence. In correspondence of four craters (indicated by white arrows) the structures verge in the opposite direction (see text for more details). On the background is a MDIS BDR mosaic (166 *m*/pixel) in equirectangular projection.

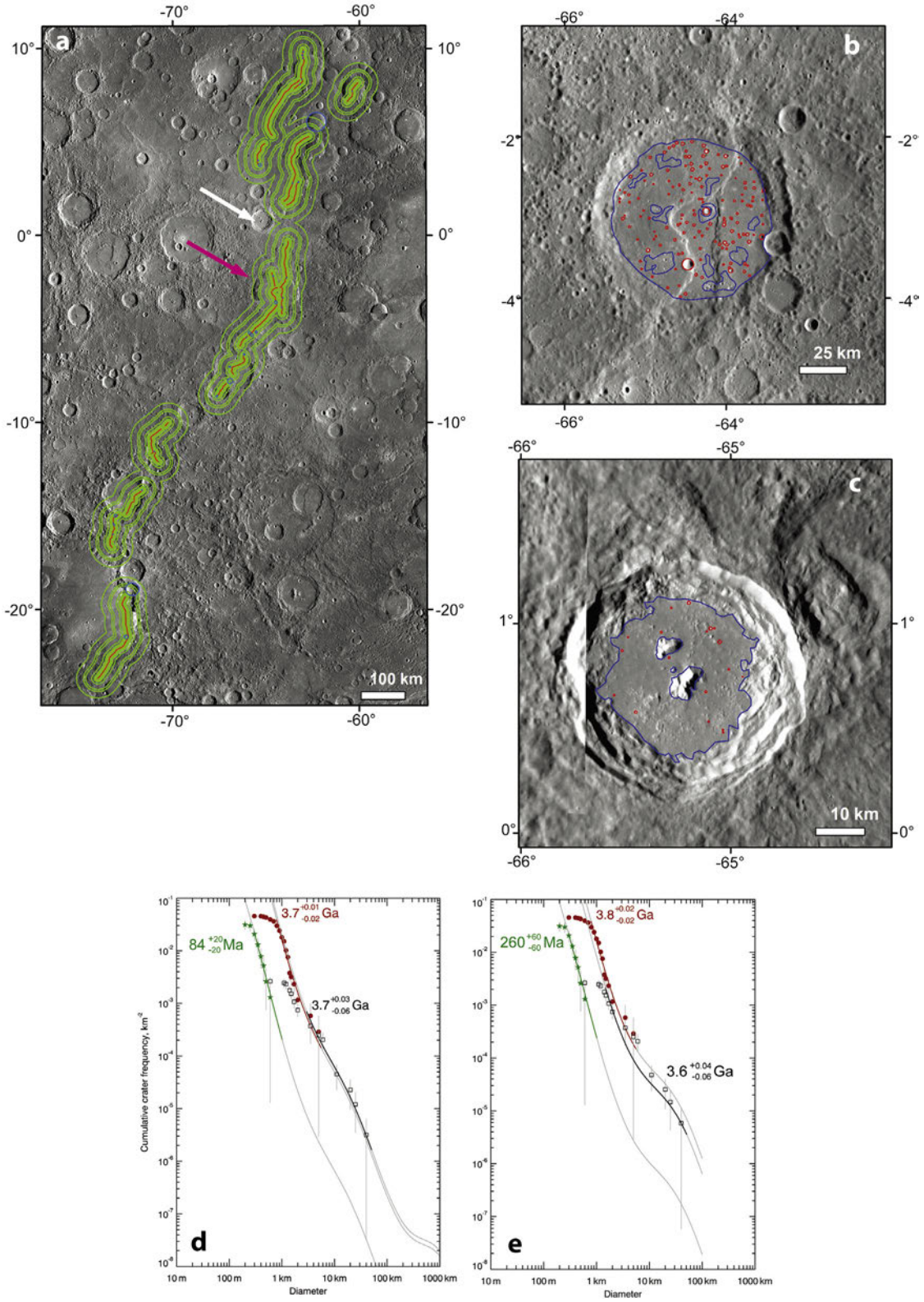

Fig. 3. Dating of Thakur thrust system. (a) Buffer areas (in green) created around lineaments (in red). Blue circles indicate the crater overlapping the structures and considered in the count to compile the final crater SFD and date the system. A faulted and an unfaulted crater were also chosen to estimate a maximum and a minimum age limit for the system and are indicated by a pink and a white arrow, respectively. (b) Enlarged view of Thakur crater. In blue are outlined the area chosen for the counting and in red are the counted craters. (c) Enlarged view of the chosen unfaulted crater (unnamed); the count was performed on a NAC image (EN1053868463 M; 87 *m*/pixel). Symbology as in (b). The crater SFDs of the system (black squares), of Thakur crater (red filled circles), and the unfaulted crater (green filled stars) were plotted and compared with LWPF porous scaling law (d), and NPF (e) to obtain the absolute model age for the system.

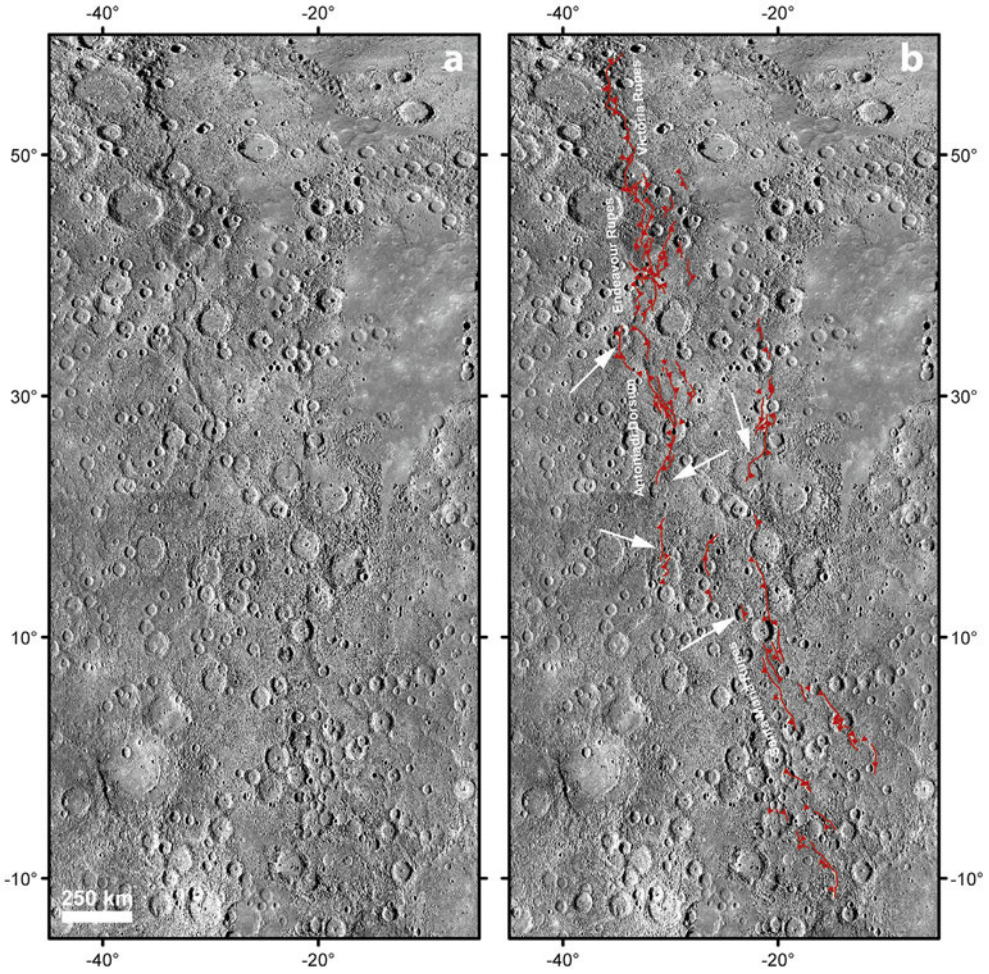

Fig. 4. (a) Victoria thrust system, named after Victoria rupes, the longest scarp encompassed in the system. (b) Structures composing the system are outlined in red (triangles indicate the dip direction of the thrust). The system shows an eastward vergence. In correspondence of five craters (indicated by white arrows), the structures show an opposite vergence (see text for more details). On the background is a MDIS BDR mosaic (166 *m*/pixel) in equirectangular projection.

correspondence of four craters (i.e. Thakur crater, and three unnamed craters, Fig. 2), the thrusts show an opposite vergence. The southernmost lobate scarp constituting the system is a basin-edge lobate scarp formed at the edge of a smooth plain infilling the 340 km diameter Raphael basin.

3.1.1. *Thakur system's age*

A total amount of 30 craters overlapping Thakur system were counted (Fig. 3a). By comparing the CSFD with the LWPF the age obtained for the thrust is 3.7 (+0.03/–0.06) Ga (Fig. 3d).

By considering the NPF we obtain 3.6 (+0.04/–0.06) Ga, which is concordant with the age gained with LWPF (Fig. 3e).

To obtain the maximum age limit for the system's activity we choose to date the floor of Thakur crater, which is filled with a smooth plain deformed by structures (Fig. 3b).

The age obtained with LWPF is 3.7 (+0.01/–0.02) Ga, suggesting a sin-deformational origin for the crater (Fig. 3d). Following NPF, we obtained instead an age of 3.8 ± 0.02 Ga (Fig. 3e).

To obtain a minimum age for the system's activity we need to date an unfaulted crater. However, the craters overlaying structures are not large enough to perform CSFD measurements, or their floor is covered by clusters of secondary craters. Therefore, we chose to date the floor of a crater located at about 50 km from the system but whose ejecta clearly mantle the north-central structures. The crater, 50 km in diameter, shows a very sharp morphology, a very smooth floor and extended ejecta (Fig. 3c). As expected, the crater floor results very young: 84 ± 20 Ma according to LWPF (Fig. 3d). By using NPF we obtained instead an older age of 260 ± 60 Ma (Fig. 3e). The time span provided is quite wide suggesting that the crater formed well after the end of thrust system activity.

3.2. *Victoria system (extended)*

This system is located between 65.00°N and 11.52°S and 35.92°W and 10.87°W. It represents the longest system considered in this work covering a length of about 3500 km from the northern to the southern end (Fig. 4). The northern part (encompassed between 58°24′N and 22°N) is based on the geological map of Galluzzi et al. (2016) and has been already analyzed by Galluzzi et al. (2019). In this work we considered also the southern extension of the system. The overall system is constituted by forty-eight mapped thrusts, crossing in large part heavily cratered intercrater plains. The longest thrust within the system is the 550 km-long Victoria Rupes, from which we took the name for the system as a whole. Other long lobate scarps are included in the system, as Antoniadi Dorsum, Endeavour and Santa Maria rupes (Fig. 4b). The structures included in the system show a prevalent N–S orientation in the northern and central sector, changing slightly to NNW–SSE toward south to return N–S at the southern tip. Some of the thrusts follow the crater rims, suggesting that they developed along previous impact discontinuities. The system verges mainly toward east, although several changes in vergence are locally observable. In fact, in correspondence of the central and southern part of the system some back thrusts are observed in

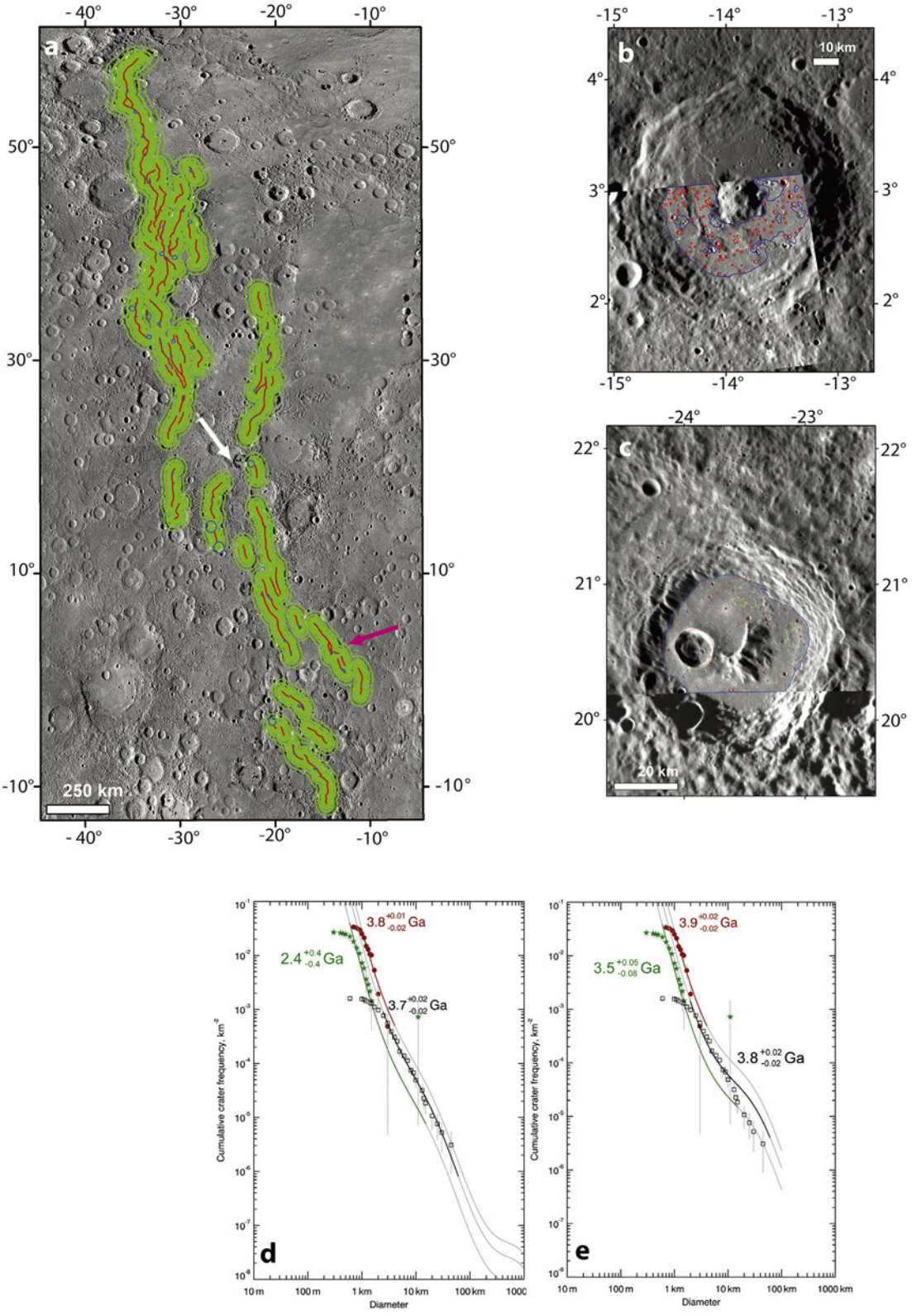

Fig. 5. Dating of Victoria thrust system. (a) Buffer areas (in green) created around lineaments (outlined in red). Craters overlapping the structures and considered for the counting are outlined in blue. A pink and a white arrow respectively indicate a faulted and an unfaulted crater chosen to estimate a maximum and a minimum age limit for the system. (b) Enlarged view of the faulted crater (unnamed). In blue are outlined the area chosen for the counting and in red are the counted craters. Count was performed on a NAC image (EN1022397268 M; 58 *m*/pixel). (c) Enlarged view of the chosen unfaulted crater (unnamed). Symbology as in (b). Count was made on EN1067811079 M NAC image (91 *m*/pixel). The crater SFDs of the system (black squares), of the faulted crater (red filled circles), and unfaulted crater (green filled stars) were plotted and compared with LWPF porous scaling law (d), and NPF (e) to obtain the absolute model age for the system. NPF chart shows a depletion of larger craters. This is possibly due to an underestimation of craters larger than 20 km superposed to the thrust system, although such depletion seems to not be observed on LWPF chart.

association with the main thrust. Moreover, like in the case of Thakur system, the structures show opposite vergence in correspondence with five craters (Fig. 4).

3.2.1. Victoria system's age

In order to date the Victoria system 114 craters were counted (Fig. 5a). We then obtained an age of about 3.7 (±0.02) Ga for LWPF. With NPF we obtained an age similar to the first case, attested at 3.8 ± 0.02 Ga (Fig. 5d and e).

To obtain a maximum age limit of the system's activity we chose a faulted central peak crater named Donne, of about 85 km in diameter (Fig. 5b). We chose it among the other faulted craters since its floor does not appear to be affected by ejecta of surrounding craters, and then the effect of secondaries on the age estimation should be minimized. The crater count of the floor gave a maximum age limit of 3.8 (+0.01/–0.02) Ga with LWPF, similar to the 3.9 ± 0.02 Ga obtained with NPF (Fig. 5d and e respectively).

The superposed craters that are suitable to obtain the minimum age limit for Victoria system (i.e. with a crater floor large enough for a good statistic and not affected by secondaries) were lacking. For this reason, we choose a central peak crater that does not directly overlap the structures but lays over a 25 km-diameter crater whose rim covers a structure located in the central part of the system. The chosen crater has a diameter of 67 km and shows a well preserved rim and clearly visible proximal ejecta (Fig. 5c). The crater counting of the crater's floor gave an age of 2.4 ± 0.4 Ga with LWPF (Fig. 5d). With NPF the age was instead 3.5 (+0.05/–0.08) Ga (Fig. 5e).

3.3. Villa Lobos system

The system is located between 23.63°N and 1.95°N and 3.45°E and 15.28°E for a maximum N–S extent of about 900 km (Fig. 6). It encompasses twenty-five thrusts, one of them cutting the Villa Lobos crater. Therefore, we refer here to the system as Villa Lobos system.

It shows a general N–S orientation with a westward vergence. Such a vergence is kinematically in agreement with the slight change in trend of the southern structures (NW–SE), likely representing lateral ramps of the system, linked with the frontal thrust. In correspondence with three unnamed craters (Fig. 6) thrusts show an opposite vergence. In two of these craters thrusts are observed to follow crater margins, suggesting that they follow pre-existing zones of weakness. Back-thrusts are detected in association to some of the main faults, frequently in the eastern part of the system. The thrust system cuts a variety of terrains, from intercrater plains to large craters filled with smooth plains. The eastern part of the system, in particular, cuts an extended less cratered region, likely the result of a resurfacing process.

3.3.1. Villa Lobos system's age

For Villa Lobos system 18 craters were considered for the BCC (Fig. 7a). The end of activity of the system has been dated at about 3.6 (+0.09/–0.8) Ga with LWPF, an age similar to that obtained with NPF, attested at about 3.6 (+0.06/–0.01) Ga (Fig. 7d and e).

For the maximum age limit we dated the floor of a large faulted crater with a diameter of about 120 km, located in the central sector of the system. It shows a moderately degraded crater rim and proximal ejecta (Fig. 7b). We obtained an age of 3.7 (+0.02/–0.03) Ga with LWPF and

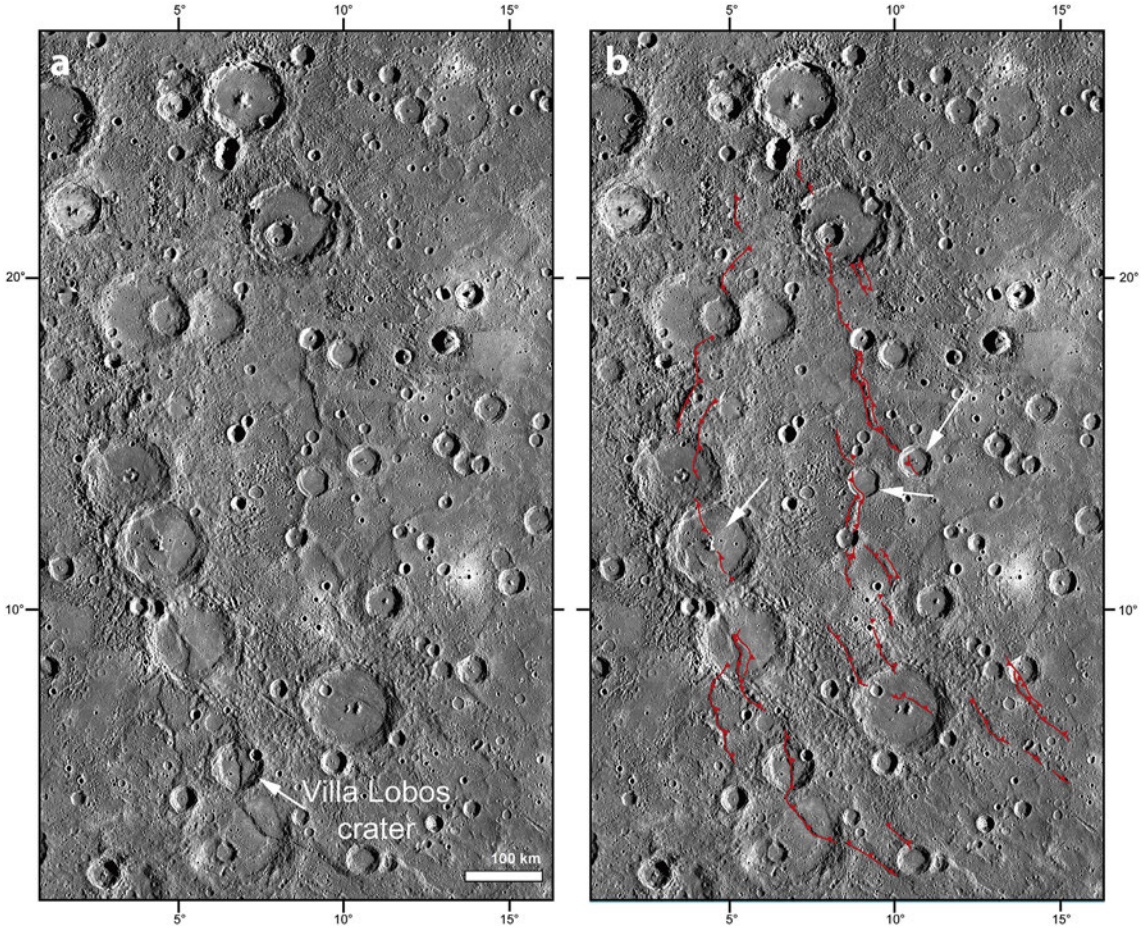

Fig. 6. Villa Lobos thrust system, named after Villa Lobos crater (a). (b) Structures encompassed in the system, outlined in red (triangles indicate the dip direction of the thrust), show a prevalent westward vergence. In association with three craters (indicated by white arrows), the structures show an opposite vergence (see text for more details). On the background is a MDIS BDR mosaic (166 *m*/pixel) in equirectangular projection.

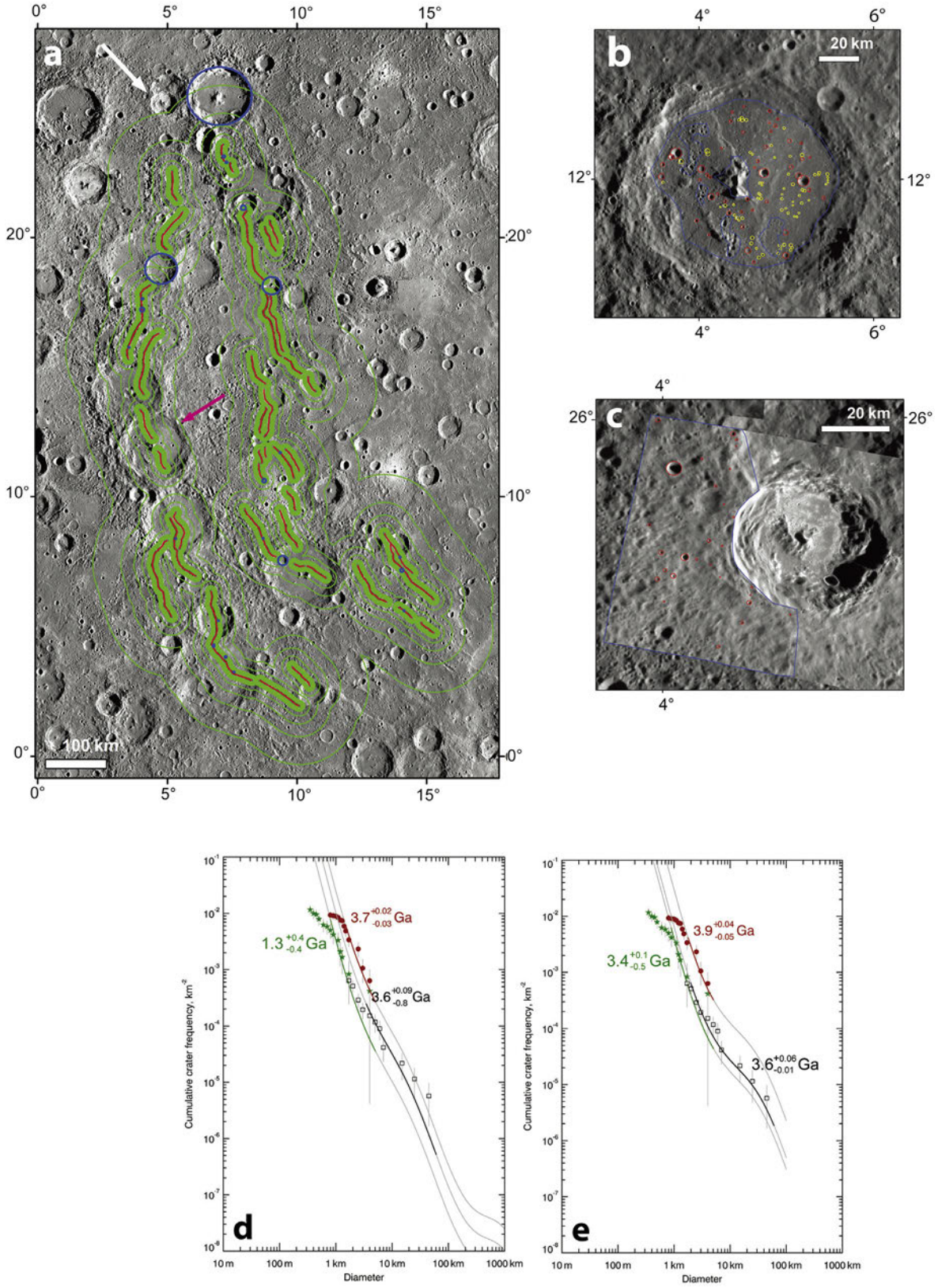

Fig. 7. Dating Villa Lobos thrust system. (a) Buffer areas (in green) created around lineaments (outlined in red). Craters overlapping the structures and considered for the counting are outlined in blue. A pink arrow indicates the faulted crater chosen for the maximum system's age limit; white arrow indicates Kyosai crater, chosen to estimate the minimum limit. (b) Enlarged view of the faulted crater (unnamed) showing the area chosen for the counting (outlined in blue) and the counted craters. In red are the primary craters considered for the count, in yellow the secondaries which were excluded from the count. (c) Enlarged view of Kyosai crater. The count was performed on a NAC image (EN0220675399 M; 65 *m*/pixel). Symbology as in (b). The crater SFDs of the system (black squares), of the faulted crater (red filled circles), and of Kyosai crater (green filled stars) were plotted and compared with LWPF porous scaling law (d), and NPF (e) to obtain the absolute model age for the system.

3.9 (+0.04/–0.05) Ga with NPF (Fig. 7d and e, respectively).

Concerning the minimum age limit, the superposed craters larger enough to be suitable for a traditional CSFD measurement were very few. One of the larger superposed crater located in the northern sector of the system has the floor heavily affected by chains or clusters of craters, likely due to the ejecta of subsequent craters. The presence of such secondary craters could invalidate the count. Then, we decided to consider a crater named Kyosai (Fig. 7c), located immediately on the west side of this larger crater and whose ejecta superpose its rim. However, the floor of Kyosai shows extended areas of hollows. Therefore, the age of this surface can be compromised. For this reason the ejecta of the crater were considered for CSFD measurements, obtaining and absolute model age of 1.3 ± 0.4 Ga, following LWPF (Fig. 7d). Following instead NPF, the age gap between the final stage of the system activity and the superposed crater is shorter, since the model assigns an age of 3.4 (+0.1/–0.5) Ga (Fig. 7e).

3.4. Al-Hamadhani system

This thrust system extends between 42.63°N and 12.02°N and 99.44°W and 83.22°W and includes twenty-four structures, for a total length of about 1500 km. One of its lobate scarps cuts a crater named Al-Hamadhani, from which the system has been named (Fig. 8).

The lobate scarps crosscut intercrater plains but also several large basins whose floor is covered by smooth plains.

In the south-western part, the lobate scarps also cut an extended area characterized by a lower crater density with respect to the surrounding area and which is probably constituted by volcanic deposits as well.

The system shows a general NE–SW orientation and a vergence toward NW. Also in this system, structures with opposite vergence (i.e. SE) have been observed on five unnamed craters. Locally, the main thrust is associated with back-thrusts, in particular approaching some of the crater rims.

3.4.1. Al-Hamadhani system's age

To determine an absolute model age for the Al-Hamadhani system 43 craters were included in the BCC measurement (Fig. 9a). The BCC method established the final stage of the activity at about 3.7 (+0.02/–0.03) Ga for LWPF (Fig. 9d). An age of 3.8 ± 0.03 Ga was obtained instead with NPF (Fig. 9e).

The maximum age limit for system's activity was derived by counting the floor of a large faulted crater, 116 km in diameter, showing signs of erosion but with a still preserved crater rim and remnants of the ejecta blanket (Fig. 9b). We obtained an age of about 3.8 (+0.01/–0.02) Ga following LWPF (Fig. 9d); NPF gave an age of 3.9 (+0.02/–0.03) Ga (Fig. 9e).

To obtain the minimum age limit, we dated the ejecta of a crater with a diameter of 30 km that overlays the central segment of the system. It shows a well preserved rim, a central peak and proximal ejecta (Fig. 9c). The count gave an age of 100 ± 40 Ma for LWPF (Fig. 9d), with NPF we obtained instead an age of 300 ± 100 Ma (Fig. 9e). Also in this case the time span between the age of the final stage of thrust's activity and the minimum age limit is considerably wide.

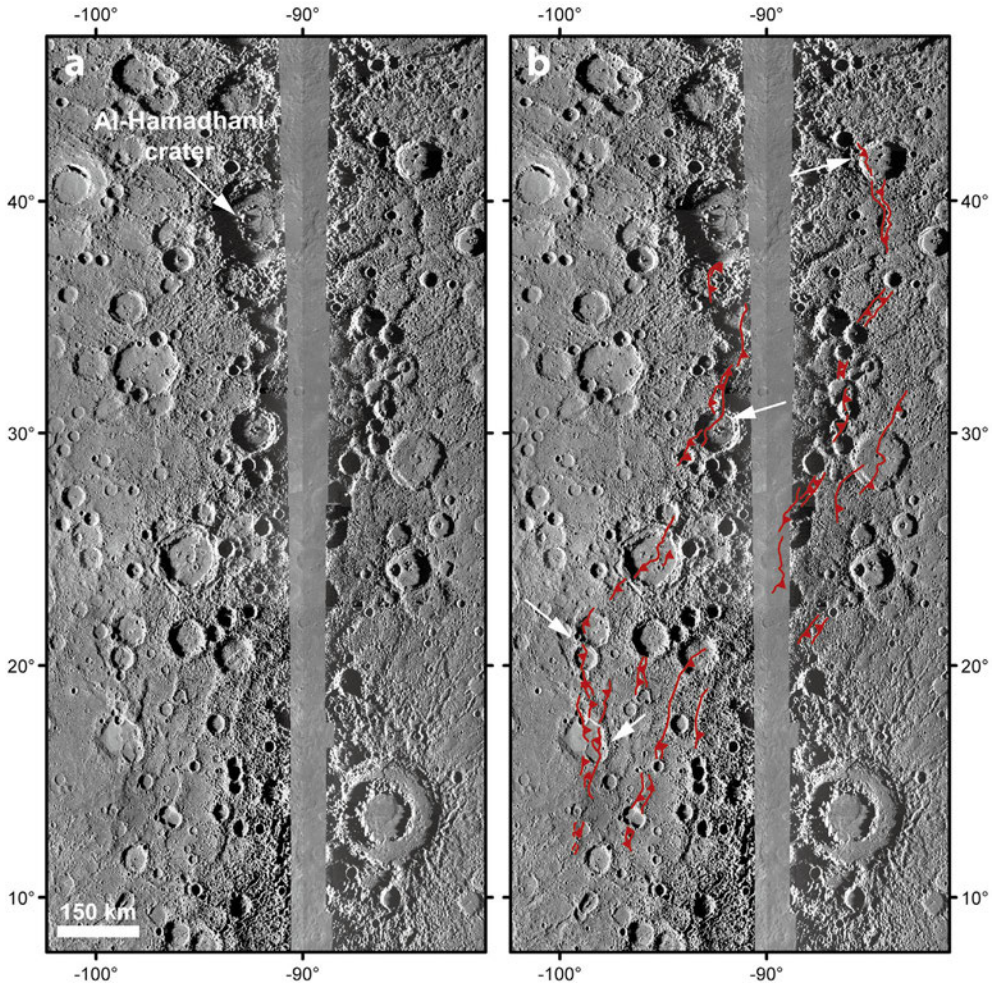

Fig. 8. (a) Al-Hamadhani thrust system, named after Al-Hamadhani crater. (b) Structures encompassed in the system (in red; triangles indicate the dip direction of the thrust), verge toward NW. Opposite vergence was observed in correspondence of four craters (indicated by white arrows; see text for more details). On the background is a MDIS high solar incidence angle BDR mosaics (on the left: HIWmosaic; on the right: HIE mosaic; the grey stripe in the center of the image is due to the different illumination conditions of the images used for the mosaics) (166 *m*/pixel) in equirectangular projection.

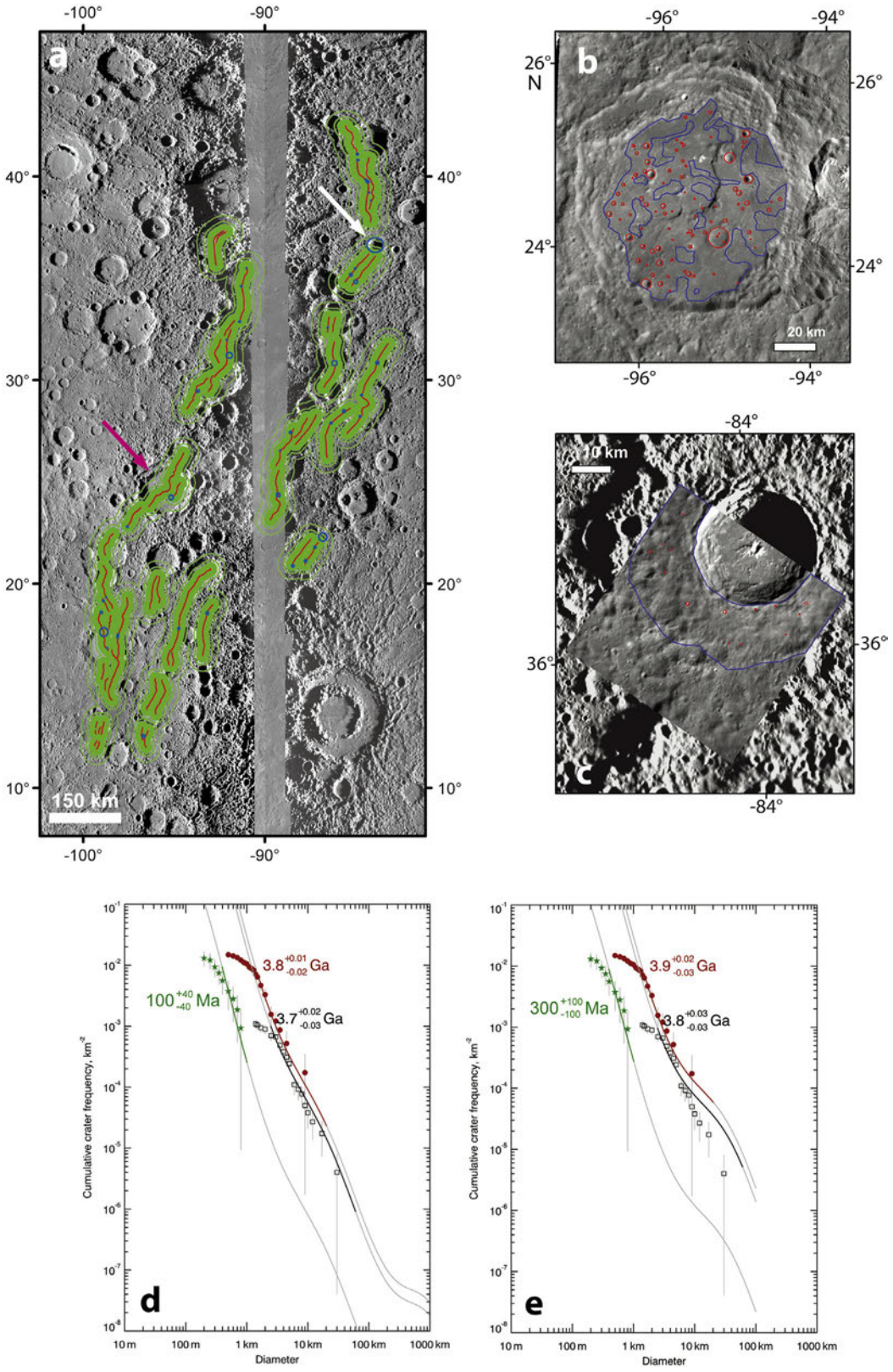

Fig. 9. Dating Al-Hamadhani thrust system. (a) Buffer areas (in green) created around lineaments (outlined in red). Craters overlapping the structures and considered for the counting are outlined in blue. The faulted and the unfaulted craters are indicated by a pink and a white arrow, respectively. (b) Enlarged view of the faulted crater (unnamed) showing the area chosen for the counting (outlined in blue) and the counted craters (in red). (c) Enlarged view of the unfaulted crater (unnamed). The count was performed on a NAC image (EN0211416032 M; 100 *m*/pixel). Symbology as in (b). The crater SFDs of the system (black squares), of the faulted crater (red filled circles), and unfaulted crater (green filled stars) were plotted and compared with LWPF porous scaling law (d), and NPF (e) to obtain the absolute model age for the system.

3.5. Enterprise system

This thrusts system represents the surface expression of a large-scale thrust fault (Fig. 10). Topographic and kinematic analyses attest that this system includes Enterpise Rupes, one of the longest thrust known on Mercury (Watters et al., 2009a; Ferrari et al., 2015; Massironi et al., 2015), from which we took our name for the system. It is located between 25.47°S and 38.68°S and 64.89°E and 84.23°E, for a total length of 820 km. This system transects the Rembrandt basin and includes two segments, one inside and one outside the crater, which show different characteristics. Indeed, on the western branch, outside the basin, the system has a WSW–ENE orientation whereas on the eastern branch, in the basin's floor, the orientation changes in SW–NE (Ferrari et al., 2015; Galluzzi et al., 2015). Several strike-slip kinematic indicators have been observed along the thrusts suggesting a dextral transpression in the western branch and a sinistral transpression in the eastern one. This, coupled with the arcuate shape in plan view and the asymmetric relief of the thrusts, indicates a SE vergence for the Enterprise system (Galluzzi et al., 2015; Massironi et al., 2015).

The system crosses different types of material: from heavily cratered terrains, outside the Rembrandt basin, to smooth plains within the Rembrandt basin.

3.5.1. Enterprise system's age

The craters counted to date the Enterprise system are 22 (Fig. 11a). The age obtained with LWPF for the Enterprise system is 3.7 (+0.03/–0.04) Ga (Fig. 11d). By following NPF we obtain an age of 3.8 (+0.05/–0.08) Ga (Fig. 11e).

The maximum age limit can be provided by the Rembrandt basin. As highlighted by Ferrari et al. (2015), Rembrandt inner plains are constituted by different subunits. Therefore, a CSFD of the Rembrandt floor would not be representative of the younger resurfacing event alone, but of more than one event. For this reason we chose to date the Rembrandt basin itself. Ferrari et al. (2015) already performed the crater counting for the Basin related Material (BM) that includes the basin's proximal ejecta and hummocky unit, interpreted to be a mixture of impact melt and ejecta (Fig. 11b). The age obtained for BM was 3.85 ± 0.1 Ga, following NPF (Fig. 11f). In this work we considered the same crater count, obtaining a comparable age of 3.8 ± 0.007 Ga for the LWPF (Fig. 11d).

For the minimum age the only superposing crater whose floor is big enough to be dated is located in the northern sector of Enterprise Rupes. It has a diameter of about 23 km and shows a sharp morphology (Fig. 11c). The result of the crater count gave an age of 950 ± 200 Ma with LWPF (Fig. 11d) and 2.0 ± 0.4 Ga (Fig. 11f) following NPF (Fig. 11e).

4. Discussion

The results obtained with the BCC technique revealed that the systems taken into account in this work ended their activity into a time range of 3.6–3.7 Ga, following LWPF, and 3.6–3.8 Ga, considering NPF. A further discussion about the age differences observed between LWPF and NPF is included in the supplementary material.

The results obtained for the thrust systems are in agreement with the age estimated previously for other Mercurian systems, as the Blossom thrust system, whose activity was estimated to end at about 3.5–3.7 Ga, according to the Model Production Function (cohesive soil) proposed by Marchi et al. (2009) and NPF, respectively (Giacomini et al., 2015). Addition of the Blossom system to the five systems reported here allows a more complete global assessment of major tectonic systems that occurred on Mercury (see the "Graphical abstract").

These results are also in agreement with the classical stratigraphic analysis between lobate scarps and craters performed by Banks et al. (2015). They estimated that the fault activity should have occurred by a time near to the Late Heavy Bombardment (LHB) (i.e. an increasing of impacts registered on lunar surface probably due to an injection in the inner system of main belt and/or Kuiper belt objects, occurred at about 4.0 Ga according to Marchi et al., 2013). In fact, they observed that some lobate scarps appear superposed by undeformed Calorian craters (Calorian system covers a time span between 3.9 Ga and 3.5–3.0 Ga). Banks et al. (2015) also observed that some lobate scarps continue their activity until recent age, since some small (<3 km) fresh craters appear modified or cut by scarps. This is in agreement with the discovery of some thrusts interpreted to be Kuiperian in age on the basis of crater degradation morphologies (Watters et al., 2015). Such a long-lived tectonic activity is not in contrast with our results since the ages we obtained using the BCC method for each system represent the final major activity recorded for the system as a whole, but more recent movements could have been occurred in some single thrusts.

Anyway, the results suggest that the tectonic activity giving rise to lobate scarps took place very early in Mercury's history, well before than previously hypothesized by thermophysical models (Tosi et al., 2013). According to these models, the tectonism of Mercury is intimately related with the beginning of the contraction of the planet due to the core's cooling process. This contraction has been estimated to start at about 3

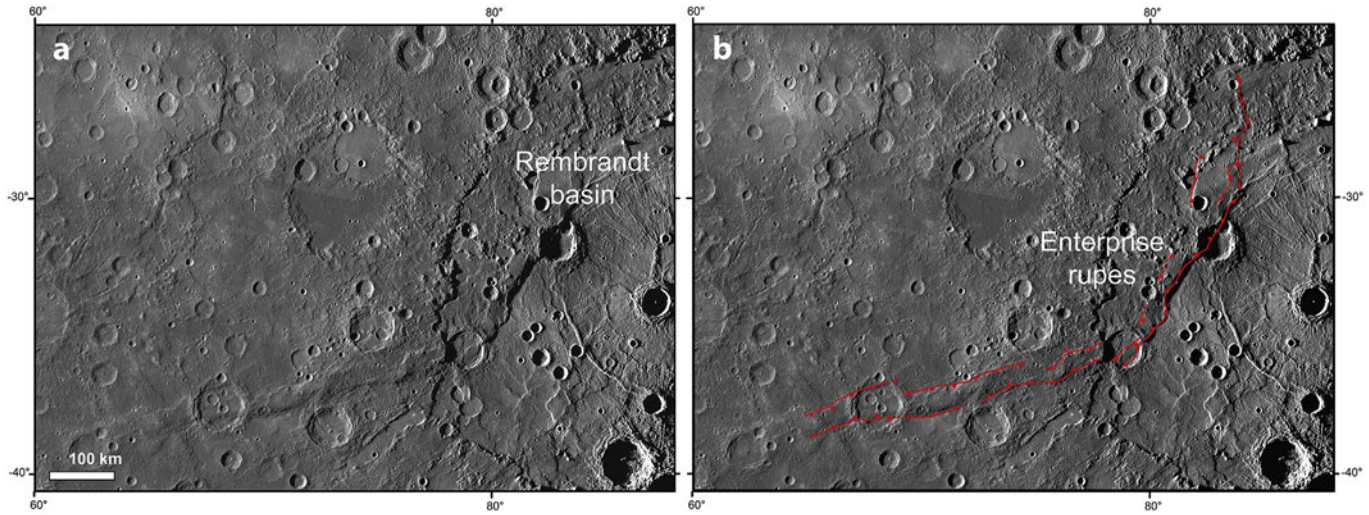

Fig. 10. (a) Enterprise system named after Enterprise rupes. (b) The system's structures, outlined in red (triangles indicate the dip direction of the thrust), verge toward SE (see text for more details). On the background is a MDIS high solar incidence angle BDR mosaic (166 *m*/pixel) in equirectangular projection.

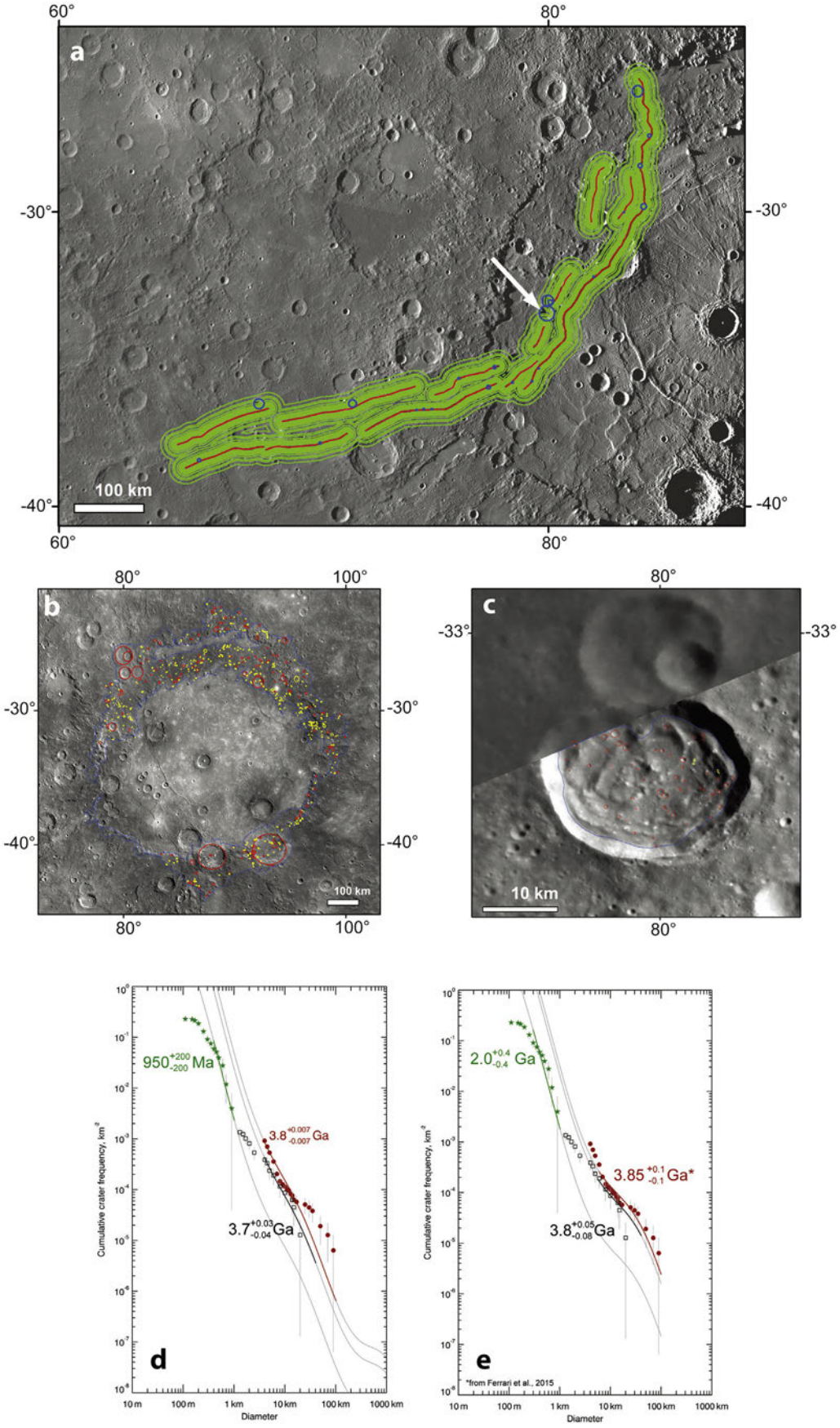

Fig. 11. Dating Enterprise thrust system. (a) Buffer areas (in green) created around lineaments (outlined in red). Craters overlapping the structures and considered for the counting are outlined in blue. White arrow indicates the unfaulted crater chosen for the minimum system's age limit estimation. (b) Rembrandt basin was chosen for the maximum age limit. The area considered for the count is outlined in blue. In red are the primary craters considered for the count, in yellow the secondaries, excluded from the count. (c) Enlarged view of the unfaulted crater (unnamed). The count was performed on a NAC image (EN1059205122 M; 49 *m*/pixel). The crater SFDs of the system (black squares), of the Rembrandt basin (red filled circles), and unfaulted crater (green filled stars) were plotted and compared with LWPF porous scaling law (d), and NPF (e) to obtain the absolute model age for the system. The steepening observed in the NPF chart for the smaller craters can be due to the presence of possible secondary craters since the counted area includes the basin proximal ejecta, where secondaries could be formed during the impact that formed the basin itself.

Ga, well after the LHB (Grott et al., 2011; Tosi et al., 2013). Our results, however, would suggest that the activity responsible for the lobate scarps growth began earlier in Mercury's history, at least before 3.6 Ga.

This means that the actual thermal model for the planet should be modified changing some parameters, like mantle temperature and viscosity or thickness of the regolith layer, in order to allow an earlier contraction.

On the other hand, the results obtained in this work could suggest that these major thrust systems formed in response to other processes, like tidal despinning (e.g. Klimczak et al., 2015), but also mantle downwelling (Massironi et al., 2015; Watters et al., 2015), which then could have played a role on the structures formation and then on Mercury's evolution.

Such hypothesis seems to be confirmed also by the age estimated for the extended smooth plains, which assesses the end of the widespread effusive volcanism at about 3.5 Ga (Byrne et al., 2016). Indeed, the end of the extensive volcanism corresponds with the progressive contraction of the crust and the consequent closure of the conduits that allow the rising of magma toward the surface. Therefore, large volume effusive volcanism is not expected to occur after the beginning of the global contraction (Wilson and Head, 2008; Byrne et al., 2016). However, this is not in agreement with the age obtained in this work for the end of thrust system's activity (3.6–3.7 Ga). Then, if the beginning of the contraction occurred after 3.5 Ga, as suggested by the thermophysical models and Byrne et al.'s results, it is likely that the thrust systems considered in this work formed in response to other processes.

Moreover, the thrust systems are mainly located in the lower latitudes and show a prevalent N–S orientation (see Fig. 1 and the Graphical abstract), in accordance with the scenario predicted by Klimczak et al. (2015) that, on the basis of stress' magnitude and latitudinal variation, theorized a higher density and larger dimension of structures at the equatorial zone. Furthermore, the systems show a concentration in longitudinal bands, in agreement with Watters et al. (2015) that observed a non-uniform spatial and aerial distribution of the largest tectonic structures. It seems also that the systems show a regular longitudinal framework. Such a pattern could represent evidence that mantle convection, with regularly-spaced linear convection planforms, could have been involved in the first stages of Mercury's evolution, as suggested by King (2008). Alternatively, it can be expression of variations on the lithospheric strength (Watters et al., 2015).

The detection of strike-slip kinematic indicators, that cannot be explain with the solely contraction, seems to confirm the hypothesis that other mechanisms should be invoked to explain the Mercury's tectonic framework (Massironi et al., 2015).

5. Conclusions

Five long thrust systems have been identified and dated through the buffered crater counting (BCC) technique in order to temporally constrain their activity. Two different chronology models were adopted: LeFeuvre and Wieczorek Production Function and the Neukum Production Function. For the former an age ranging between 3.6 Ga and 3.7 Ga (porous scaling law) was obtained, whereas for the latter one a slightly wider range of 3.6–3.8 Ga has been estimated. To date the systems, only unfaulted craters were counted, therefore the age obtained indicate the final stage of the activity registered along the thrust systems, when the associated stress was insufficient to cause the deformation of craters located along their strike. The resulted thrusts systems' ages are coherent with the classical stratigraphic approach, as they are set between the faulted and unfaulted crater's age. That comparability would support the effectiveness of the BCC technique as a method to date thrust systems. Such results have important implications regarding the thermal evolution of Mercury since they provide new clues on what occurred during the first stage of the planet's history. Indeed, their early formation (well before than predicted by the thermophysical models), the chronological relationships with widespread effusive volcanism, their non-random orientation and spatial distribution, suggest that they can be formed with the contribution of other processes beside global contraction. This leads us to hypothesize that mantle downwelling or tidal despinning, could have contribute to the planet's evolution.

A significant finding is that all the thrust systems ended their activity at about the same time, rather early on the planet evolution. This would suggest that the higher strains exceeding the frictional resistance of the lithosphere, causing the surface breaking at large scale (and then the formation of systems of thrusts) occurred prevalently early in the planet history. This seems in agreement with hypothesis that higher strain rate occurred on Mercury prior to 3.9–3.5 Ga, and decreased over the time (Phillips and Solomon, 1997; Klimczak, 2015).

Declaration of interest statement

The authors declare that they have no known competing financial interests or personal relationships that could have appeared to influence the work reported in this paper.

Acknowledgments

We thank A. Nahm, J. Clark and an anonymous reviewer who provided detailed and helpful suggestions that improved the quality of the manuscript. Part of this work was funding from the Italian Space Agency (ASI) under ASI-INAF agreement 2017-47-H.0.

Appendix A. Supplementary data

Supplementary data to this article can be found online at https://doi.org/10.1016/j.gsf.2019.09.005.

References

Banks, M.E., Xiao, Z., Watters, T.R., Strom, R.G., Braden, S.E., Chapman, C.R., Solomon, S.C., Klimczak, C., Byrne, P.K., 2015. Duration of activity on lobate-scarp thrust faults on Mercury. J. Geophys. Res. Planets 120 (11), 1751–1762.
Beuthe, M., 2010. East–west faults due to planetary contraction. Icarus 209, 795–817.
Bouley, S., Craddock, R.A., Mangold, N., Ansan, V., 2010. Characterization of fluvial activity in Parana Valles using different age-dating techniques. Icarus 207 (2), 686–698.
Burns, J.A., 1976. Consequences of the tidal slowing of Mercury. Icarus 28, 453–458.
Byrne, P.K., Klimczak, C., Şengör, A.M.C., Solomon, S.C., Watters, T.R., Hauck, S.A., 2014. Mercury's global contraction much greater than earlier estimates. Nat. Geosci. 7, 301–307.
Byrne, P.K., Ostrach, L.R., Fassett, C.I., Chapman, C.R., Denevi, B.W., Evans, A.J., Klimczak, C., Banks, M.E., Head, J.W., Solomon, S.C., 2016. Widespread effusive volcanism on Mercury likely ended by about 3.5 Ga. Geophys. Res. Lett. 43 (14), 7408–7416.
Clark, J.D., Hurtado Jr., J.M., Hiesinger, H., Bernhardt, H., van der Bogert, C.H., 2017. Investigation of lobate scarps: implications for the tectonic and thermal evolution of the Moon. Icarus 298, 78–88.
Denevi, B.W., Ernst, C.M., Meyer, H.M., Robinson, M.S., Murchie, S.L., Whitten, J.L., Head, J.W., Watters, T.R., Solomon, S.C., Ostrach, L.R., Chapman, C.R., Byrne, P.K., Klimczak, C., Peplowski, P.N., 2013. The distribution and origin of smooth plains on Mercury. J. Geophys. Res. Planets 118, 891–907.
Dombard, A.J., Hauck, S.A., 2008. Despinning plus global contraction and the orientation of lobate scarps on Mercury. Icarus 198, 274–276.
Dzurisin, D., 1978. The tectonic and volcanic history of Mercury as inferred from studies of scarps, ridges, troughs, and other lineaments. J. Geophys. Res. 83, 4883–4906.
Fassett, Caleb I., Head, James, W., 2008. Valley network-fed, open-basin lakes on Mars: distribution and implications for Noachian surface and subsurface hydrology. Icarus 198, 37–56.
Fegan, E.R., Rothery, D.A., Marchi, S., Massironi, M., Conway, S.J., Anand, M., 2017. Late movement of basin-edge lobate scarps on Mercury. Icarus 288, 226–234.
Ferrari, S., Massironi, M., Marchi, S., Byrne, P.K., Klimczak, C., Martellato, E., Cremonese, G., 2015. Age relations of Rembrandt basin and Enterprise rupes, Mercury. In: Platz, T., Massironi, M., Byrne, P.K., Hiesinger, H. (Eds.), Volcanism and Tectonism across the Inner Solar System, vol 401. Geol. Soc. London Spec. Pub., pp. 159–172
Giacomini, L., Massironi, M., Marchi, S., Fassett, C.I., Di Achille, G., Cremonese, G., 2015. Age dating of an extensive thrust system on Mercury: implications for the planet's thermal evolution. In: Platz, T., Massironi, M., Byrne, P.K., Hiesinger, H. (Eds.), Volcanism and Tectonism across the Inner Solar System, vol 401. Geol. Soc. London Spec. Pub., pp. 291–311
Galluzzi, V., Di Achille, G., Ferranti, L., Popa, C., Palumbo, P., Platz, T., Massironi, M., Byrne, P.K., Hiesinger, H., 2015. Faulted craters as indicators for thrust motions on

Mercury. In: Volcanism and Tectonism across the Inner Solar System, vol 401. Geol. Soc. London Spec. Pub, pp. 313–325.
Galluzzi, V., Guzzetta, L., Ferranti, L., Di Achille, G., Rothery, D.A., Palumbo, P., 2016b. Geology of the Victoria quadrangle (H02), Mercury. J. Maps 12, 227–238.
Galluzzi, V., Ferranti, L., Massironi, M., Giacomini, L., Guzzetta, L., Palumbo, P., 2019. Structural analysis of the Victoria quadrangle fault systems on Mercury: timing, geometries, kinematics and relationship with the high-Mg region. J. Geophys. Res. Planets. https://doi.org/10.1029/2019JE005953.
Gault, D.E., Guest, J.E., Murray, J.B., Dzurisin, D., Malin, M.C., 1975. Some comparisons of impact craters on Mercury and the Moon. J. Geophys. Res. 80 (1975), 2444–2460.
Grott, M., Breuer, D., Laneuville, M., 2011. Thermo-chemical evolution and global contraction of Mercury. Earth Planet. Sci. Lett. 307 (1), 135–146.
Hartmann, W.K., 1977. Relative crater production rates on planets. Icarus 31, 260–276.
Hauck, S.A., Dombard, A.J., Phillips, R.J., Solomon, S.C., 2004. Internal and tectonic evolution of Mercury. Earth Planet. Sci. Lett. 222, 713–728.
Hoke, M.R.T., Hynek, B.M., 2009. Roaming zones of precipitation on ancient Mars as recorded in valley networks. J. Geophys. Res. 114 https://doi.org/10.1029/2008JE003247.
Holsapple, K.A., 1993. The scaling of impact processes in planetary sciences. Annu. Rev. Earth Planet Sci. 21, 333–373. A94-10876 01-91.
Holsapple, K.A., Housen, K.R., 2007. A crater and its ejecta: an interpretation of deep impact. Icarus 187, 345–356.
King, S.D., 2008. Pattern of lobate scarps on Mercury's surface reproduced by a model of mantle convection. Nat. Geosci. 1, 229–232.
Klimczak, C., Byrne, P.K., Solomon, S.C., 2015. A rock-mechanical assessment of Mercury's global tectonic fabric. Earth Planet. Sci. Lett. 416, 82–90.
Klimczak, C., 2015. Limits on the brittle strength of planetary lithospheres undergoing global contraction. J. Geophys. Res.: Plan 120 (12), 2135–2151.
Kneissl, T., van Gasselt, S., Neukum, G., 2011. Map-projection-independent crater size-frequency determination in GIS environments — new software tool for ArcGIS. Planet. Space Sci. 59, 1243–1254. https://doi.org/10.1016/j.pss.2010.03.015, 2011.
Kneissl, T., Michael, G.G., Platz, T., Walter, S.H.G., 2015. Age determination of linear surface features using the Buffered Crater Counting approach - case studies of the Sirenum and Fortuna Fossae graben systems on Mars. Icarus 250, 384–394.
Le Feuvre, M., Wieczorek, M.A., 2011. Nonuniform cratering of the Moon and a revised crater chronology of the inner Solar System. Icarus 214 (1), 1–20.
Marchi, S., Mottola, S., Cremonese, G., Massironi, M., Martellato, E., 2009. A new chronology for the Moon and Mercury. Astron. J. 137, 4936–4948.
Marchi, S., Chapman, C.R., Fassett, C.I., Head, J.W., Bottke, W.F., Strom, R.G., 2013. Global resurfacing of Mercury 4.0–4.1 billion years ago by heavy bombardment and volcanism. Nature 499, 59–61. https://doi.org/10.1038/nature12280.
Massironi, M., Di Achille, G., Rothery, D., Galluzzi, V., Giacomini, L., Ferrari, S., Zusi, M., Cremonese, G., Palumbo, P., 2015. Lateral ramps and strike-slip kinematics on Mercury. In: Platz, T., Massironi, M., Byrne, P.K., Hiesinger, H. (Eds.), Volcanism and Tectonism across the Inner Solar System, vol. 401. Geol. Soc. London Spec. Pub., pp. 269–290
Matsuyama, I., Nimmo, F., 2009. Gravity and tectonic patterns of Mercury: effect of tidal deformation, spin–orbit resonance, nonzero eccentricity, despinning and reorientation. J. Geophys. Res. 114, E01010. https://doi.org/10.1029/2008JE003252.
Melosh, H.J., Dzurisin, D., 1978. Mercurian global tectonics - a consequence of tidal despinning. Icarus 35, 227–236.
Melosh, H.J., 1977. Global tectonics of a despun planet. Icarus 31, 221–243.
Melosh, H.J., McKinnon, W.B., 1988. The tectonics of Mercury. In: Vilas, F., Chapman, C.R., Matthews, M.S. (Eds.), Mercury. The University of Arizona Press.
Melosh, H.J., 1989. Impact Cratering: A Geologic Process. Oxford University Press, New York, p. 245.
Melosh, H.J., Ivanov, B.A., 1999. Impact crater collapse. Annu. Rev. Earth Planet Sci. 27, 385–415.
Michael, G.G., Neukum, G., 2010. Planetary surface dating from crater size-frequency distribution measurements: partial resurfacing events and statistical age uncertainty. Earth Planet. Sci. Lett. 294 (3–4), 223–229.
Neukum, G., 1983. Meteoriten bombardement und Datierung planetarer Ober flachen. Habilitation, University of Munich, February (in German).
Neukum, G., Ivanov, B., 1994. Crater Size distributions and impact probabilities on earth from lunar, terrestrial-planet, and asteroid cratering data. In: Gehrels, Tom, Matthews, M.S., Schumann, A. (Eds.), Hazards Due to Comets and Asteroids, Space Science Series, vol 1994. University of Arizona Press, Tucson, AZ, p. 359.
Neukum, G., Ivanov, B.A., Hartmann, W.K., 2001a. Cratering records in the inner solar system in relation to the lunar reference system. Space Sci. Rev. 96, 55.
Neukum, G., Oberst, J., Hoffmann, H., Wagner, R., Ivanov, B.A., 2001b. Geologic evolution and cratering history of Mercury. Planet. Space Sci. 49 (14–15), 1507–1521.
Pechmann, J.B., Melosh, H.J., 1979. Global fracture patterns of a despin planet application to Mercury. Icarus 38, 243–250.
Phillips, R.J., Solomon, S.C., 1997. Compressional strain history of Mercury. In: 28th Annual Lunar and Planetary Science Conference, LPI Contribution, 1572, pp. 1107–1108.
Pike, R.J., 1978. Geomorphology of impact craters on Mercury. In: Vilas, F., Chapman, C.R., Matthews, M.S. (Eds.), Mercury. Univ. Arizona PressAriz, Tucson, pp. 165–273.
Platz, T., Michael, G., Tanaka, K.L., Skinner, J.A., Fortezzo, C.M., 2013. Crater-based dating of geological units on Mars: methods and application for the new global geological map. Icarus 225, 806–827.
Schubert, G., Ross, M.N., Stevenson, D.J., Spohn, T., 1988. Mercury's thermal history and the generation of its magnetic field. In: Vilas, F., Chapman, C.R., Matthews, M.S. (Eds.), Mercury. The University of Arizona Press.
Schultz, R.A., 1993. Brittle strength of basaltic rock masses with applications to Venus. J. Geophys. Res. 98 (E6), 10883–10895.
Senthil Kumar, P., Sruthi, U., Lakshmi, K.J.P., Menon, R., Amitabh Krishna, B.G., Kring, D.A., Head, J.W., Goswami, J.N., Kumar, A.S.K., 2016. Recent shallow moonquakes and impact-triggered boulder falls on the Moon: new insights from the Schrödinger basin. J. Geophys. Res. 121, 147–197.
Solomon, S.C., 1976. Some aspects of core formation in Mercury. Icarus 28, 509–521.
Solomon, S.C., 1977. The relationship between crustal tectonics and internal evolution in the Moon and Mercury. Phys. Earth Planet. Inter. 15, 135–145.
Strom, R.G., Trask, N.J., Guest, J.E., 1975. Tectonism and volcanism on Mercury. J. Geophys. Res. 80, 2478–2507.
Strom, R.G., Neukum, G., 1988. The cratering record on Mercury and the origin of impacting objects. In: Vilas, F., Chapman, C.R., Matthews, M.S. (Eds.), Mercury. The University of Arizona Press, pp. 336–373.
Strom, R.G., Banks, M.E., Chapman, C.R., Fassett, C.I., Forde, J.A., Head, J.W., Merline, W.J., Prockter, L.M., Solomon, S.C., 2018. Mercury crater statistics from MESSENGER flybys: implications for stratigraphy and resurfacing history. Planet. Space Sci. 59 (15), 1960–1967.
Tanaka, K.L., 1982. A new time-saving crater-count technique with application to narrow features. NASA Tech. Memo. 123–125. TM-85127.
Tosi, N., Grott, M., Plesa, A.-C., Breuer, D., 2013. Thermochemical evolution of Mercury's interior. J. Geophys. Res.: Plan 118 (12), 2474–2487.
van der Bogert, C.H., Hiesinger, H., Dundas, C.M., Krüger, T., McEwen, A.S., Zanetti, M., Robinson, M.S., 2017. Origin of discrepancies between crater size-frequency distributions of coeval lunar geologic units via target property contrasts. Icarus 298, 49–63.
van der Bogert, C.H., Clark, J.D., Hiesinger, H., Banks, M.E., Watters, T.R., Robinson, M.S., 2018. How old are lunar lobate scarps? 1. Seismic resetting of crater size-frequency distributions. Icarus 306, 225–242.
Watters, T.R., Robinson, M.S., Cook, A.C., 1998. Topography of lobate scarps on Mercury: new constraints on the planet's contraction. Geology 26, 991–994.
Watters, T.R., Solomon, S.C., Robinson, M.S., Head, J.W., André, S.L., Hauck II, S.A., Murchie, S.L., 2009a. The tectonics of Mercury: the view after MESSENGER's first flyby. Earth Planet. Sci. Lett. 285, 283–296.
Watters, T.R., Murchie, S.L., Robinson, M.S., Solomon, S.C., Denevi, B.W., André, S.L., Head, J.W., 2009b. Emplacement and tectonic deformation of smooth plains in the Caloris basin Mercury. Earth Planet. Sci. Lett. 285 (3–4), 309–319.
Watters, T.R., Nimmo, F., 2010. Tectonism on Mercury. In: Schultz, R.A., Watters, T.R. (Eds.), Planetary Tectonics. Cambridge Univ Press, pp. 15–80.
Watters, T.R., Selvans, M.M., Banks, M.E., Hauck, S.A., Becker, K.J., Robinson, M.S., 2015. Distribution of large-scale contractional tectonic landforms on Mercury: implications for the origin of global stresses. Geophys. Res. Lett. 42 (10), 3755–3763.
Wichman, R.W., Schultz, P.H., 1989. Sequence and mechanisms of deformation around the Hellas and Isidis impact basins on Mars. J. Geophys. Res. 94, 17333–17357.
Wilson, L., Head, J.W., 2008. Volcanism on Mercury: a new model for the history of magma ascent and eruption. Geophys. Res. Lett. 35 (23). CiteID L23205.
Xiao, Z., 2018. On the importance of self-secondaries. Geoscience Letters 5, 17. https://doi.org/10.1186/s40562-018-0116-9.
Yue, Z., Michael, G.G., Di, K., Liu, J., 2017. Global survey of lunar wrinkle ridge formation times. Earth Planet. Sci. Lett. 477, 14–20.